PHYSICAL REVIEW E **87**, 022205 (2013)

Role of collisions in erosion of regolith during a lunar landing

Kyle J. Berger,[1] Anshu Anand,[1] Philip T. Metzger,[2] and Christine M. Hrenya[1,*]
[1]*Department of Chemical and Biological Engineering, University of Colorado, Boulder, Colorado 80303, USA*
[2]*NASA Kennedy Space Center, Granular Mechanics and Regolith Operations Laboratory, Kennedy Space Center, Florida 32899, USA*

(Received 11 September 2012; published 19 February 2013)

The supersonic gas plume of a landing rocket entrains lunar regolith, which is the layer of loose solids covering the lunar surface. This ejection is problematic due to scouring and dust impregnation of surrounding hardware, reduction in visibility for the crew, and spoofing of the landing sensors. To date, model predictions of erosion and ejection dynamics have been based largely on single-trajectory models in which the role of interparticle collisions is ignored. In the present work, the parameters affecting the erosion rate of monodisperse solids are investigated using the discrete element method (DEM). The drag and lift forces exerted by the rocket exhaust are incorporated via one-way coupling. The results demonstrate that interparticle collisions are frequent in the region immediately above the regolith surface; as many as 20% of particles are engaged in a collision at a given time. These collisions play an important role both in the erosion dynamics and in the final trajectories of particles. In addition, a direct assessment of the influence of collisions on the erosion rate is accomplished via a comparison between a "collisionless" DEM model and the original DEM model. This comparison shows that the erosion dynamics change drastically when collisions are considered and that the erosion rate is dependent on the collision parameters (coefficient of restitution and coefficient of friction). Physical explanations for these trends are provided.

DOI: 10.1103/PhysRevE.87.022205 PACS number(s): 45.70.−n, 47.11.Mn

I. INTRODUCTION

When a rocket lands on the Moon, the supersonic rocket exhaust plume (hereafter referred to as the gas plume) causes the regolith, or soil-like particles, to be lifted from the surface [1–4]. Such ejection of regolith can be problematic due to scouring and dust impregnation of surrounding hardware, reduction in crew visibility, and spoofing of landing sensors [5–7].

The ejection process is different from analogous terrestrial gas-solid flows in several ways. First, the gas plume from the rocket is characterized by high Knudsen and high Mach number conditions. Also, in the high velocity/high shear of a rocket exhaust, aerodynamics (lift and drag) dominate over gravity within the locality of the lander where the erosion is taking place. Thus, particles never fall back to the surface in the region of interest and saltation does not occur apart from interparticle collisions occurring above the surface. In addition, particles are easily lifted off the surface in this case by the strong plume even in the absence of saltating splashes to mechanically eject them from the surface. This case of lift and drag dominance over gravity occurs not only with rocket exhaust, but also in cases with sufficiently strong subsonic impinging jets forming scour holes in a granular material, which is relevant to some terrestrial processes (i.e., scour holes forming under a culvert discharging water, or in a pneumatic excavation using gas jets) [8]. The case of aerodynamic dominance is different than the most commonly studied case of Aeolian sand transport where gravity and saltation dominate [9–14]. In addition, the lack of atmosphere on the Moon results in an absence of drag once the particles leave the influence of the gas plume. Gravity is also reduced compared to a flow in terrestrial conditions. Finally, the particle size distribution (PSD) is much wider than soil found on Earth; i.e., the bulk of regolith particles fall within the range of 0.001–10 mm.

Due to these differences between the erosion of lunar soil compared to its terrestrial counterpart, the dominant physical mechanisms may differ between the two environments, and hence so may the resulting phenomenology, scaling relationships, etc. An understanding of the mechanisms of such erosion across a wider range of conditions is needed prior to the development of more detailed simulations to support planetary science or space mission engineering. This first step, namely to identify important physics at play in lunar soil ejection and evaluate the corresponding impact on erosion rate, is the focus of the current effort.

Before describing previous work related to regolith ejection, it is helpful to define a few key terms. *Surface erosion*, or just *erosion*, refers to the process of particles being lifted from the regolith surface by the gas plume. The rate at which this happens is known as the *erosion rate*. *Ejection dynamics* refers to what happens to the regolith particles after they leave the surface.

Previous work on predicting the surface erosion and ejection dynamics of lunar regolith relies largely on *single-particle trajectory models* [15–17] coupled with computational fluid dynamics (CFD) and a simple erosion rate model [8]. This combined treatment is known as the plume erosion trajectory (PET) model. First, the gas plume (the P of PET) is simulated using CFD and the resulting shear stress on the surface of the regolith is calculated. The erosion rate is then calculated using dimensionless scaling laws (the E of PET) to compare the shear stresses calculated (using the CFD model above) and the erosion rates observed for the Apollo landings. The trajectories of different size particles (the T of PET) from each point of erosion are then calculated one at a time. For each particle, its acceleration and velocity are found by integrating its aerodynamic (drag and lift) and gravitational forces through

---

[*] Corresponding author: hrenya@colorado.edu

the gas flow field under the assumption that no particle-particle contacts are occurring. The ejection pattern can then be calculated by scaling the flux at a given point by the erosion rate. Nonetheless, previous investigations into the erosion phenomenon have suggested that particle-particle collisions, which are neglected in the above model, may play a role in erosion and ejection dynamics. For example, both experiments and examination of Apollo landing videos [18] suggest that collisions are frequent and significantly affect both the erosion rate and ejection dynamics. Furthermore, pieces of the Surveyor III returned from the Moon have been investigated using scanning electron microscopy and energy dispersive x-ray spectroscopy, and it has been concluded that interparticle collisions were responsible for the Surveyor being bombarded by regolith [19]. More specifically, the Surveyor was shielded by the lunar terrain, and thus only particles knocked below the main regolith spray by collisions would have had an opportunity to collide with the Surveyor. In addition, the authors show evidence of clusters of particles colliding with the Surveyor, a well-known granular phenomenon which can only be predicted by models that include interparticle collisions [20,21]. Even in the case of terrestrial erosion dominated by saltation and gravity, interparticle mid-air collisions have been shown to have a significant effect on the erosion [11–14]. Namely, mid-air collisions may result in a decrease in the number of saltating particles and thus reduce erosion rate, which in turn reduces the number of mid-air collisions. In an aerodynamic dominated erosion regime, the erosion will be much faster and thus mid-air collisions will play an even greater role.

To better understand and begin to quantify the role of collisions on the erosion of regolith, the discrete element method (DEM) is used here to simulate the surface erosion of lunar regolith. The DEM simulations track individual particle motion according to Newton's laws, including forces arising from one-way particle-gas coupling (gas affects particles but not vice versa), lunar gravity, and collisions. As a first step, the erosion of a monodisperse collection of spheres is considered in a semiperiodic box under the influence of an external fluid velocity field. The results demonstrate that collisions are numerous, with as many as 20% of eroded particles engaged in a collision at a given time, and that such collisions significantly impact the erosion rate.

II. COMPUTATIONAL MODEL

A. System description

Figure 1 shows a simplified schematic of the system. The impingement point is the point on the lunar surface directly below the landing rocket. The gas plume first contacts the regolith in the vertical direction at the impingement point as seen in Fig. 1, and then the gas plume spreads outward in the radial direction. The computational domain investigated here is located at a distance of 6 m from the impingement point in the radial direction. The computational domain, which is depicted as a gray box in Fig. 1, is illustrated in greater detail in Fig. 2. The domain is a three-dimensional rectangular box with periodic boundary conditions in the x and z directions. The predominant direction of the gas plume is radially outwards from the impingement point, i.e., in the positive x direction. The simplification of using a rectangular box, as opposed to a radial wedge, is done since the width (z direction) is much smaller than the circumference of a circle with a diameter of 6 m. The domain contains a collection of monodisperse spheres, which differs from actual lunar soil but is appropriate for this initial model because it is the simplest model for which collisions can be observed. Once the collisions in this system have been studied, the more complex cases of polydispersity and nonspherical particles can be examined.

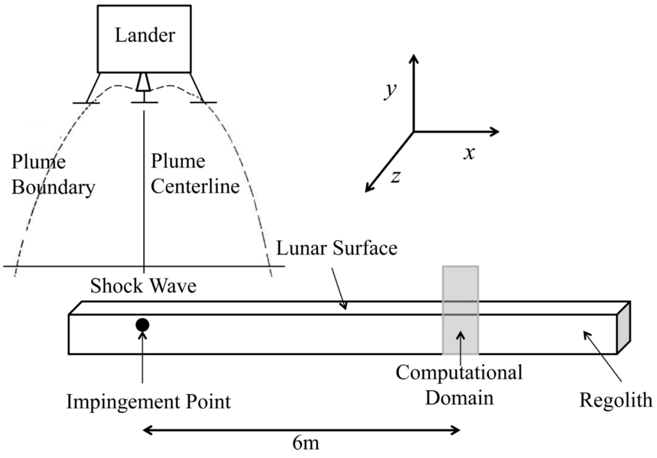

FIG. 1. Illustration showing the location of computational domain with respect to the impingement point.

To characterize the erosion process as a function of time, two planes are defined in the computational domain, as displayed in Fig. 2. First, the anchoring plane represents the (assumed) depth to which the gas plume penetrates the regolith layer. The assumption of a penetrating depth is a practical consideration in this simplified model to ensure gas forces are adequate to lift particles from the bed in the absence of saltation splashes, which is the case of interest as observed in experiments [8,18]. The penetration represents the grain-scale details of the gas flow under and around the individual particles on the surface of the bed as well as the time-varying turbulent interactions with the bed, details that are omitted for simplicity in this first model. The anchoring plane divides the regolith into two parts: the perturbed regolith and unperturbed regolith. The particles located above the anchoring plane are under the direct influence of the gas plume and thus form the perturbed regolith layer. The particles located under the anchoring plane do not experience the effects of the gas plume. Second, the erosion plane represents the position at which the erosion rate is calculated, and thus it is positioned a small distance

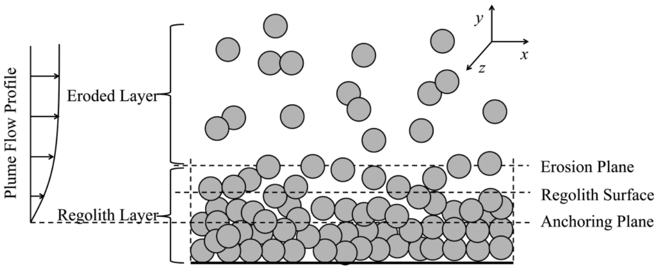

FIG. 2. Computational domain.

above the surface of the regolith layer. The erosion plane divides the computational domain into two parts: eroded layer and regolith layer. As can be seen in Fig. 2, there is a gradual transition in terms of the volume fraction between these two regions in the vertical direction.

The positions of both the anchoring and erosion planes move as the simulation progresses. Specifically, the volumetric erosion rate (i.e., the rate at which particles leave the regolith layer for the eroded layer) is calculated at every time step. The anchoring plane is then adjusted in the negative y direction until it sweeps through a volume that corresponds to the volumetric loss of particles in the previous time step, including the void space between particles in the regolith layer. In this manner, the height of the erosion plane above the surface of the regolith layer remains fixed throughout the simulation (i.e., the regolith surface and anchoring plane both move down at the same rate). The (adjusted) volumetric erosion rate also feeds into the new position of the anchoring plane. Namely, the anchoring plane is moved downward by the same distance as the erosion plane in each time step, thereby ensuring a constant penetration depth of the anchoring plane into the regolith layer throughout the simulation. Accordingly, new (deeper) layers of regolith are affected by the gas plume throughout the course of the simulation.

B. Gas-particle model

For purposes of this work, a one-way coupling between the gas plume and particles is assumed. Specifically, the gas plume affects the particles (via a lift and drag force), but the particles do not affect the plume. This simplifying assumption of one-way coupling is used as a first step since the analysis of the effects of two-way coupling on the gas plume itself is beyond the scope of this work. Additionally, no studies have been performed on how the particles affect the gas plume at conditions similar to those present on the Moon. As detailed below, the gas plume is described by computational fluid dynamics (CFD) simulations and the particles are described via the discrete element method (DEM).

1. Gas plume model

The flow of the rocket exhaust plume was modeled using the computational fluid dynamics package FLUENT. The CFD was performed in two dimensions (axisymmetric) using the Spalart-Allmaras turbulent model (the renormalization group k-ε model was also used for comparison). The parameters used for the CFD can be found in Table I. The plume profile developed from the CFD simulations is then used as an input to the DEM simulations. Figure 3(a) gives the variation of the radial plume velocity at a distance of 6 m from the impingement point and as a function of distance from the surface of the regolith as calculated from the CFD analysis. Only the bottom portion of this plot where the velocity increases with height, which is expanded and illustrated in Fig. 3(b), is used in the DEM studies reported here since we are interested in the behavior near the surface. In Fig. 3(a), note that the velocity monotonically increases until a certain height (∼0.80 m), after which the velocity begins to decrease with height. A decrease in gas velocity with an increase in height will cause negative lift (lift in the downward direction) and thus the ejection dynamics may change near this height. However, because this study is only focused on the initial stages of the erosion dynamics, the portion of the velocity profile that will cause a negative lift is at a vertical distance too large to be important.

TABLE I. Parameters for CFD simulations of gas plume.

Property	Value
Specific heat (constant pressure)	1610 J/K kg
Thermal conductivity	0.0777 W/m K
Dynamic viscosity	9.568×10^{-5} Pa s
Molecular weight	20.8 g/mole
Ambient pressure	0.1 Pa

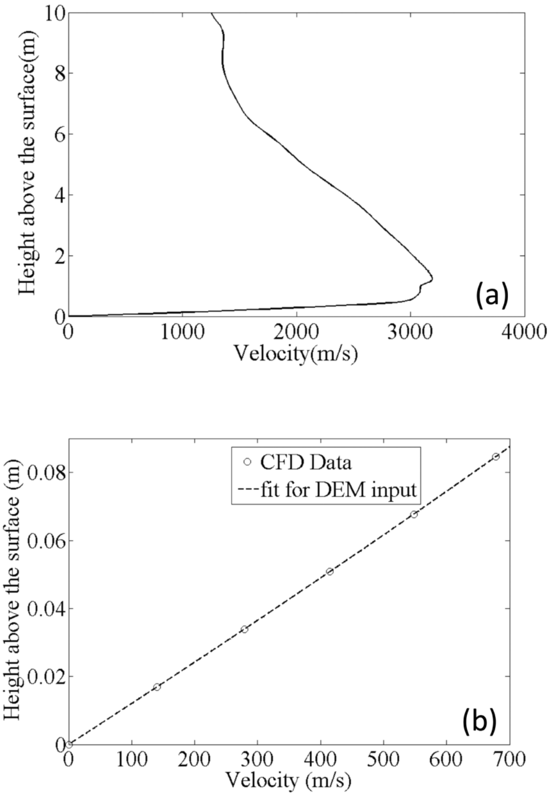

FIG. 3. (a) Radial plume velocity determined from CFD simulations at a distance of 6 m from the impingement point as a function of distance from the surface of the regolith. (b) Subset of same radial plume velocity profile used in the DEM studies.

2. DEM (particle model)

The regolith particles are modeled as inelastic, frictional spheres using DEM. An in-house DEM code was developed using a soft-sphere methodology [22]. This code was verified with a general-purpose code developed by NETL (National Energy Technology Laboratory) called MFiX (Multiphase Flow with Inter-phase eXchanges [29]). All results presented here are those obtained using the in-house code.

The acceleration, **a**, of the particle at any given time step is related to the total force on a particle $\mathbf{F}_{\text{total}}$ as follows:

$$m\mathbf{a} = \mathbf{F}_{\text{total}} = \mathbf{F}_{\text{weight}} + \mathbf{F}_{\text{Coll}} + \mathbf{F}_{\text{Drag}} + \mathbf{F}_{\text{Lift}}, \tag{1}$$

TABLE II. Baseline parameters.

Particle Properties	Value
Total number, n	800
Diameter, d	0.1 cm
Density, ρ	2.7 $\mathrm{g/cm^3}$
Time step, Δt	$\sim 6 \times 10^{-7}$ s
Plume Properties	Value
Material density, ρ_g	1.27×10^{-3} $\mathrm{g/cm^3}$
Viscosity, μ	1.983×10^{-4} $\mathrm{dyn/cm^2}$ s
Temperature, T_∞	500 K
Lunar Conditions	Value
Acceleration due to gravity on the Moon	163 $\mathrm{cm/s^2}$
Particle Collision Properties	Value
Spring stiffness	
particle-particle	
normal, $k_{\mathrm{norm,pp}}$	8 000 000 $\mathrm{g/s^2}$
tangential, $k_{\mathrm{tan,pp}}$	8 000 000 $\mathrm{g/s^2}$
particle-wall	
normal, $k_{\mathrm{norm,pw}}$	8 000 000 $\mathrm{g/s^2}$
tangential, $k_{\mathrm{tan,pw}}$	8 000 000 $\mathrm{g/s^2}$
Friction coefficient	
particle-particle, μ_{pp}	0.20
particle-wall, μ_{pw}	0.20
Coefficient of restitution	
particle-particle, $e_{\mathrm{norm,pp}}$	0.80
particle-wall, $e_{\mathrm{norm,pw}}$	0.80
Dashpot coefficient	
normal, η_{norm}	Calculated from coefficient of restitution and spring stiffness [see Eq. (19)]
tangential, η_{tan}	$0.5\eta_{\mathrm{norm}}$
System Geometry	Value
Distance from impingement point	6 m
Length of periodic box in x direction	1.0 cm
Length of periodic box in z direction	0.5 cm
Length of box in y direction	10 000 cm
Initial bed height	1.4 cm
Initial height of anchoring plane	1.0 cm
Initial height of erosion plane	1.5 cm

where m is the mass of the particle, $\mathbf{F}_{\mathrm{weight}}$ is the force due to lunar gravity, $\mathbf{F}_{\mathrm{Coll}}$ is the contact force due to collision (contact) with other particles, and $\mathbf{F}_{\mathrm{Drag}}$ and $\mathbf{F}_{\mathrm{Lift}}$ are the drag and lift forces on the particle due to the plume (defined in the next section). $\mathbf{F}_{\mathrm{weight}}$ is given as

$$\mathbf{F}_{\mathrm{weight}} = m\mathbf{g}_{\mathrm{lunar}}, \tag{2}$$

where m is the mass of the particle and $\mathbf{g}_{\mathrm{lunar}}$ is the acceleration due to gravity on the Moon (values for all parameters are given in Table II). The angular acceleration, α, of the particle at any given time step is related to the total torque on the particle, $\boldsymbol{\tau}_{\mathrm{total}}$, as follows:

$$I\boldsymbol{\alpha} = I\frac{d\boldsymbol{\omega}}{dt} = \boldsymbol{\tau}_{\mathrm{total}} = \boldsymbol{\tau}_{\mathrm{Coll}}, \tag{3}$$

where I is the moment of inertia of the particle about its center, ω is the rotational velocity of the particle, and $\boldsymbol{\tau}_{\mathrm{Coll}}$ is the torque due to collision. A soft-sphere model with a linear spring-dashpot system is used to describe the contact forces and torques, $\mathbf{F}_{\mathrm{Coll}}$ and $\boldsymbol{\tau}_{\mathrm{Coll}}$. The total contact force on particle i due to all other particles j in contact with it is calculated as [23,24]

$$\mathbf{F}_{\mathrm{Coll},i} = \Sigma_j \mathbf{F}_{ij}. \tag{4}$$

The contact force between particles i and j, $\mathbf{F}_{ij}$, is decomposed into its normal (along the line of centers between two particles) and tangential components, $\mathbf{F}_{nij}$ and $\mathbf{F}_{tij}$, respectively, which are then further decomposed into the spring (conservative) force, $\mathbf{F}^S_{ij}$, and the dashpot (dissipative) force, $\mathbf{F}^D_{ij}$, as

$$\mathbf{F}_{nij} = \mathbf{F}^S_{nij} + \mathbf{F}^D_{nij}, \tag{5}$$

$$\mathbf{F}_{tij} = \mathbf{F}^S_{tij} + \mathbf{F}^D_{tij}. \tag{6}$$

The normal and tangential spring forces, $\mathbf{F}^S_{nij}$ and $\mathbf{F}^S_{tij}$, respectively, are calculated based on the normal overlap, $\boldsymbol{\delta}_n$, and the tangential displacement, $\boldsymbol{\delta}_t$, between the particles at a given time by

$$\mathbf{F}^{S}_{nij} = -k_{\text{norm}}\boldsymbol{\delta}_n, \tag{7}$$

$$\mathbf{F}^{S}_{tij} = -k_{\tan}\boldsymbol{\delta}_t, \tag{8}$$

where k_{norm} and $k_{\tan}$ are the normal and tangential spring constants, respectively. The normal overlap is then defined as

$$\boldsymbol{\delta}_n = \mathbf{n}_{ij}\delta_n, \tag{9}$$

where $\mathbf{n}_{ij}$ is the normal vector pointing from i to j and δ_n is the magnitude of the normal overlap. $\mathbf{n}_{ij}$ is defined as

$$\mathbf{n}_{ij} = \frac{\mathbf{x}_j - \mathbf{x}_i}{|\mathbf{x}_j - \mathbf{x}_i|}. \tag{10}$$

The magnitude of the normal overlap, δ_n, is given by

$$\delta_n = 0.5(d_i + d_j) - |\mathbf{x}_i - \mathbf{x}_j|, \tag{11}$$

where d_i and d_j are the diameters of particles i and j, respectively, and $\mathbf{x}_i$ and $\mathbf{x}_j$, are the positions of particles i and j, respectively. The tangential displacement at initiation of contact (at time t_0), $\boldsymbol{\delta}_t(t_0)$, is given by

$$\boldsymbol{\delta}_t\,(t_0) = \mathbf{v}_{tij}\min\left(\frac{|\boldsymbol{\delta}_n|}{\mathbf{v}_{ij}\cdot\mathbf{n}_{ij}}, \Delta t\right), \tag{12}$$

where $\mathbf{v}_{tij}$ is the tangential relative velocity [defined below in Eq. (13)], $\mathbf{n}_{ij}$ is the unit normal vector pointing from center of particle i to that of j, Δt is the time step, and $\mathbf{v}_{ij}$ is the relative velocity. $\mathbf{v}_{ij}$ is defined as

$$\mathbf{v}_{ij} = \mathbf{v}_i - \mathbf{v}_j, \tag{13}$$

where $\mathbf{v}_i$ and $\mathbf{v}_j$ are the velocities of particle i and j, respectively. $\mathbf{v}_{tij}$ is defined as

$$\mathbf{v}_{tij} = \mathbf{v}_{ti} - \mathbf{v}_{tj}, \tag{14}$$

where $\mathbf{v}_{ti}$ and $\mathbf{v}_{tj}$ are the tangential velocities of particle i and j, respectively.

The tangential displacement is then updated over time by

$$\boldsymbol{\delta}_t\,(t + \Delta t) = \boldsymbol{\delta}_t\,(t) + \mathbf{v}_{tij}\Delta t. \tag{15}$$

However, because the tangential displacement will not necessarily lie in the plane tangent to the particles for the duration of the collision, it is corrected by subtracting its normal component from itself via

$$\boldsymbol{\delta}_t(t + \Delta t) = \boldsymbol{\delta}_t(t + \Delta t) - [\boldsymbol{\delta}_t(t + \Delta t)\cdot\mathbf{n}_{ij}]\mathbf{n}_{ij}. \tag{16}$$

The normal and tangential dashpot force $\mathbf{F}^{D}_{nij}$ and $\mathbf{F}^{D}_{tij}$ at a given time is calculated based on the relative normal and tangential velocity, $\mathbf{v}_{nij}$ and $\mathbf{v}_{tij}$, between particles i and j, and is given by

$$\mathbf{F}^{D}_{nij} = -\eta_{\text{norm}}\mathbf{v}_{nij}, \tag{17}$$

$$\mathbf{F}^{D}_{tij} = -\eta_{\tan}\mathbf{v}_{tij}, \tag{18}$$

where η_{norm} and $\eta_{\tan}$ are normal and tangential dashpot damping coefficients. The normal dashpot damping coefficient η_{norm} is related to normal coefficient of the restitution e_{norm} and normal spring constant k_{norm} as follows:

$$\eta_{\text{norm}} = \frac{\sqrt{m_{\text{eff}}k_{\text{norm}}}\,|\ln(e_{\text{norm}})|}{\sqrt{\pi^2 + [\ln(e_{\text{norm}})]^2}}, \tag{19}$$

where m_{eff} is the effective mass of the particles in contact calculated as

$$m_{\text{eff}} = \frac{m_i m_j}{m_i + m_j}, \tag{20}$$

where m_i and m_j are the masses of particles of i and j. The torque due to collision on particle i from all other particles j in contact with i is then calculated as

$$\boldsymbol{\tau}_{\text{Coll},i} = \sum_j \boldsymbol{\tau}_{ij}, \tag{21}$$

where τ_{ij} the torque on particle i due to particle j and is calculated as

$$\boldsymbol{\tau}_{ij} = (0.5d_i - \boldsymbol{\delta}_n)(\mathbf{n}_{ij} \times \mathbf{F}_{tij}). \tag{22}$$

3. Gas-particle interaction model: Drag and lift force

The force of the plume on regolith, namely $\mathbf{F}_{\text{Drag}}$ and $\mathbf{F}_{\text{Lift}}$ in Eq. (1), is calculated using the drag and lift coefficients, respectively, developed by Loth [25,26]. The drag force is calculated in each direction depending on the relative velocity in that direction (i.e., difference between particle and gas plume velocity) and the lift force acts in the y direction (perpendicular to the gas plume velocity). The expressions of Loth were obtained using theoretical predictions and empirical corrections for an isolated, spherical particle (i.e., do not take into account the presence of surrounding particles).

Before introducing the detailed expressions provided by Loth, it is useful to discuss the range of validity of these expressions. The drag coefficient is valid for particle Reynolds numbers up to 2.0×10^5. The particle Reynolds number, Re_p, is defined as

$$\text{Re}_p = \frac{\rho v_0 d}{\mu}, \tag{23}$$

where ρ is the density of the fluid phase, v_0 is the magnitude of the relative velocity between the particle and the gas plume, d is the diameter of the particle, and μ is the viscosity of the fluid phase. The maximum particle Reynolds number present in our simulations is around 3000, which is within the range of validity for this correlation. The drag coefficient also depends on the particle Mach number and is valid up to Mach numbers of at least 10. The particle Mach number, Ma, is defined as

$$\text{Ma} = \frac{v_0}{\sqrt{\gamma RT}}, \tag{24}$$

where γ is the ratio of specific heats of the gas, R is the gas constant, and T is the temperature of the gas. The maximum particle Mach number present in our simulations is around 1.2 and is therefore within the valid range. In addition, the drag coefficient depends on the particle Knudsen number, Kn, which is defined as

$$\text{Kn} = \sqrt{\frac{\pi\gamma}{2}}\frac{\text{Ma}}{\text{Re}}. \tag{25}$$

The particle Knudsen number for our simulations is 4.4×10^{-5} (a constant for our system), which is well below the maximum valid Knudsen number, which is 100.

Similarly to the drag coefficient, the lift coefficient of Loth [25] also depends on several dimensionless groups, namely the particle Reynolds number and the continuous-phase vorticity, ω^*_{shear}, and is valid for values up to 50 and 0.8, respectively. The continuous-phase vorticity is defined as

$$\omega^*_{\text{shear}} = \left| \frac{(Dv_0)\,d}{v_0} \right|, \tag{26}$$

where (Dv_0) is the gradient of the plume velocity perpendicular to v_0 (taken to be in the vertical direction for convenience). Although the maximum particle Reynolds number in our DEM simulations is approximately 3000, the lift coefficient noted above is the best currently available for this system. However, it is not expected that using this correlation will introduce significant error because, at high particle Reynolds number, the lift coefficient does not change significantly (tends towards 0). The continuous-phase vorticity in our simulations is approximately less than 0.3, which is within the bounds for the lift correlations.

The drag force and lift force on the particle are expressed as a function of the drag and lift coefficients, C_{Drag} and C_{Lift}, and the relative unhindered velocity, $\mathbf{v}_0$, as follows:

$$\mathbf{F}_{\text{Drag}} = \frac{C_{\text{Drag}}(\pi d^2)\rho_g v_0^2}{8}\left(\frac{|\hat{\mathbf{x}}\cdot\mathbf{v}_0|}{|\mathbf{v}_0|}\right)\hat{\mathbf{x}} + \frac{C_{\text{Drag}}(\pi d^2)\rho_g v_0^2}{8} \times \left(\frac{|\hat{\mathbf{y}}\cdot\mathbf{v}_0|}{|\mathbf{v}_0|}\right)\hat{\mathbf{y}} + \frac{C_{\text{Drag}}(\pi d^2)\rho_g v_0^2}{8}\left(\frac{|\hat{\mathbf{z}}\cdot\mathbf{v}_0|}{|\mathbf{v}_0|}\right)\hat{\mathbf{z}}, \tag{27}$$

$$\mathbf{F}_{\text{Lift}} = \frac{C_{\text{Lift}}(\pi d^2)\rho_g v_0^2}{8}\,\hat{\mathbf{y}}, \tag{28}$$

where ρ_g is the plume (gas) density and $\hat{\mathbf{x}}$, $\hat{\mathbf{y}}$, and $\hat{\mathbf{z}}$ are the unit normal vectors pointing in the x, y, and z directions. The relative unhindered velocity of the particle is the velocity of the particle relative to the plume and is given as

$$\mathbf{v}_0 = \mathbf{v}_{\text{plume}} - \mathbf{v}_{\text{particle}}, \tag{29}$$

where $\mathbf{v}_{\text{particle}}$ is the velocity of the particle and $\mathbf{v}_{\text{plume}}$ is the velocity of the plume. The density of the plume is treated as a constant because it does not change significantly within the simulation domain. The detailed expressions for the drag and lift coefficients, C_D and C_L, as functions of the Reynolds, Knudsen, and Mach numbers, can be found in the Appendix.

C. Base case parameters

The simulation proceeds in two steps. First, randomly placed particles are allowed to settle in the simulation domain (see Fig. 2) under the action of lunar gravity alone (i.e., no plume effects) in order to obtain an initial settled state. Once the particles have settled, the plume velocity is turned on. In this second step, under the combined action of the plume and lunar gravity, the particles begin to erode from the regolith surface. The periodic box is chosen to be very high in the vertical (y) direction such that the effect of a "ceiling" is nonexistent (see Table II for actual lengths). The number of particles is chosen such that the erosion occurs over a sufficient amount of time to investigate the erosion and ejection dynamics near the surface. The particle size is chosen to fall within the range of particle sizes found in lunar regolith. The time step used in the simulations is chosen to be the collision time (calculated from other input parameters) divided by 50 to ensure accurate integration. The collision time, t_{col}, is given by

$$t_{\text{col}} = \pi\left[\frac{k_{\text{norm}}}{m_{\text{eff}}} - \left(\frac{\eta_{\text{norm}}}{2m_{\text{eff}}}\right)^2\right]^{-1/2}. \tag{30}$$

The initial height of the anchoring plane (see Fig. 2) is chosen to be 4 particle diameters below the top of the regolith layer to mimic the gas plume penetrating the void spaces in the bed. The initial height of the erosion plane (see Fig. 2) is chosen to be 1 particle diameter above the top of the regolith layer in order to examine the erosion very near the surface. Thus, the distance between the anchoring and erosion planes is a total of 5 particle diameters. The sensitivity of the erosion dynamics to the location of the anchoring and erosion planes is examined in Secs. III C1 and III C2. The spring constant used is typical of spring constants used in other similar DEM simulations and, as shown in Sec. III C3, the qualitative nature of our conclusions does not change with significant changes in the spring constant (several orders of magnitude) [24]. In addition, the percent overlap (relative to the particle radius), which is one possible guide for determining whether a spring coefficient is reasonable, remains below 5% (on average) for collisions near the erosion plane [27]. Perhaps more importantly, the conclusions drawn do not change with significant changes in the spring constant (see Sec. III C3).

III. RESULTS AND DISCUSSION

In the subsections below, the role of collisions will first be discussed (Sec. III A), followed by a direct comparison between DEM and single-particle trajectories via a "collisionless" DEM model (Sec. III B). Finally, the effect of input parameters will be explored (Sec. III C).

A. Base case: Impact of collisions on erosion

An important aim of this work is to assess the role of interparticle collisions on erosion and ejection dynamics near the surface. The results obtained from the base case simulation are described in detail below in order to gauge the impact of interparticle collisions. Figure 4 is a plot of the *cumulative erosion number*, which is the number of particles above the erosion plane, as a function of time after the plume is turned on at $t = 0$ s. From Fig. 4, two distinct phases are identified during the course of the simulation: the nondepleted phase and the depleted phase. The nondepleted phase corresponds to the initial section of the plot where the cumulative erosion number is increasing rapidly ($t \lesssim 0.15$ s). The depleted phase corresponds to the section of the plot with a nearly constant value of the cumulative erosion number ($t \gtrsim 0.15$ s). These phases are demarcated by the vertical dashed line in Fig. 4 as well as in subsequent figures. The depleted phase begins when all of the initially settled particles have eroded above the erosion plane and the continuous supply of particles from the regolith layer has stopped. This phase is not important to the study of the erosion because it is the result of the limited number of particles initially placed in the system.

The nondepleted phase can be further broken down into an erosion-only phase and an erosion-and-sedimentation phase (demarcated by a solid vertical line in Fig. 4). The former refers

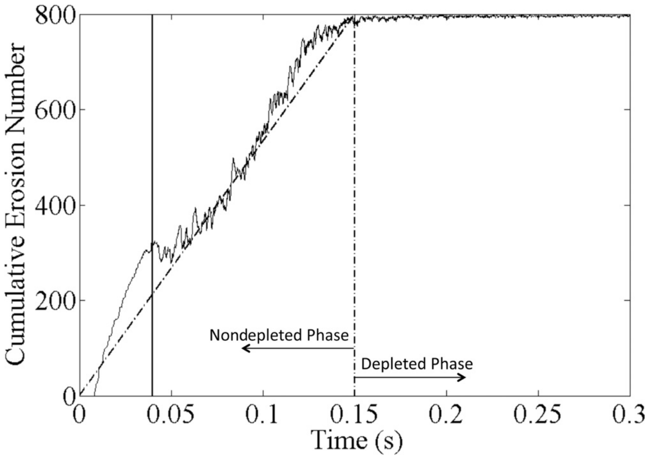

FIG. 4. Cumulative number of particles eroded as function of time for base case parameters. Dotted line denotes the average erosion during the nondepleted phase. The dashed vertical line demarcates the depleted and nondepleted phases. The solid vertical line demarcates the erosion-only and erosion-and-sedimentation phases. These lines are repeated in later plots with the same meaning.

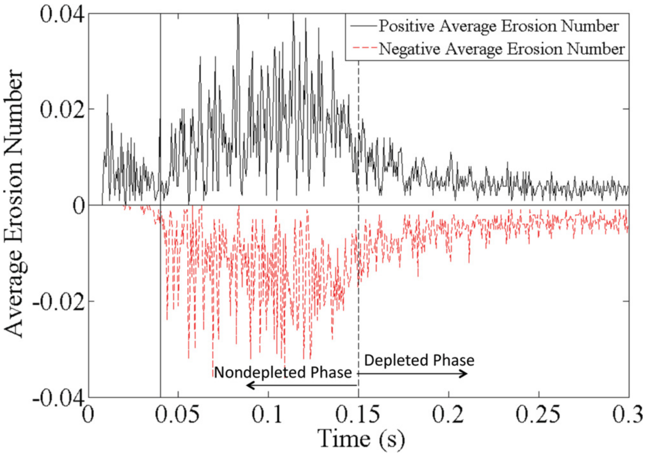

FIG. 5. (Color online) Positive and negative average erosion number (moving average of 1000 time steps).

to the portion of the plot which has no noticeable negative slope ($t \lesssim 0.04$ s) during erosion ("positive erosion" only) and the latter refers to the portion of the plot which has segments of negative slope or "negative erosion" ($t \gtrsim 0.04$ s). Even though the slopes of the two erosion phases are different, Fig. 4 includes an average fit. The slope of this fit is the overall erosion rate. The two portions of the plot have different slopes because of the nature of the beginning of the simulation. More specifically, a number of particles are immediately under the influence of the plume (as opposed to the anchoring plane gradually exposing more particles over the course of the simulation), which results in a higher initial erosion rate. However, once all of these particles have been eroded, the erosion rate decreases slightly due to particles being gradually exposed (these do not correspond exactly as there are about 220 particles in this initial region, whereas the transition occurs at around 300 particles but the sedimentation may also be playing a role in the change of erosion rate).

To give further insight into these two phases of erosion, the phenomenon of negative erosion (sedimentation) must be examined in detail. For the case of a single (isolated) particle at rest located at the surface of the regolith, that particle will only travel upward (when plume forces are "on"). This behavior is a result of the velocity monotonically increasing with height (over the length scale simulated) as evident in Fig. 3, so the lift is always positive and is typically greater than the force of gravity. The only exception is the region located approximately 1 particle diameter above the anchoring plane, but particles within this region will not move down because the stationary particles below them block downward motion. Thus, the only remaining force capable of giving rise to negative erosion is the force experienced by a particle due to collision which can cause a particle to move downward even though the lift force is greater than gravity [see Eq. (1)]. The number of collisions above the erosion plane only becomes significant after a certain time ($t \gtrsim 0.04$ s; see Fig. 6). To further understand the negative erosion of particles, the average erosion number is displayed in Fig. 5. The *average erosion number* is defined as a moving time-average, or the number of particles that cross the erosion plane per time step and averaged over 1000 time steps (1000 time steps $\sim 6 \times 10^{-4}$ s). In Fig. 5, the average erosion number has been divided into its positive contribution (average number of particles that cross the erosion plane moving up) and its negative contribution (average number of particles that cross the erosion plane moving down). As seen in this figure, there is a time lag between the first appearance of positive average erosion number ($t \sim 0.005$) and negative average erosion number ($t \sim 0.02$). Also, it is evident from this plot that the average magnitude of positive average erosion number is greater than the average magnitude of negative average erosion number. Hence, a net positive average movement of particles is observed in the positive y direction (erosion), consistent with the overall erosion rate exhibited in Fig. 4.

To better understand the collision dynamics discussed above, it is important to examine the collisions occurring above the erosion plane, since it is those collisions that result in negative erosion, whereas those below cannot contribute to negative erosion. The ratio of the moving average of the instantaneous number of collisions per time step for 1000 time steps to the number of particles above the erosion plane (at the end of the interval) is defined as the *average fractional collision number* of the system. A collision is said to happen during a given time step if two particles are overlapping at any point during that time step. The average fractional collision number is plotted in Fig. 6.

The maximum value of the average fractional collision number in Fig. 6 is approximately 0.21. Assuming that the contacts between particles are primarily binary in nature, it is evident that as many as 20% of all particles above the erosion plane are engaging in a collision at that time. In addition, after reaching a maximum value (at $t \cong 0.05$ s), the fractional collision number decreases slightly and then stays constant until the regolith layer is nearly depleted. It is interesting to note that the time at which the average fractional collision number becomes approximately constant corresponds with the first appearance of negative erosion (see Fig. 4). The leveling of the fractional collision number also appears to correspond with a similar behavior in the average erosion number (both positive and

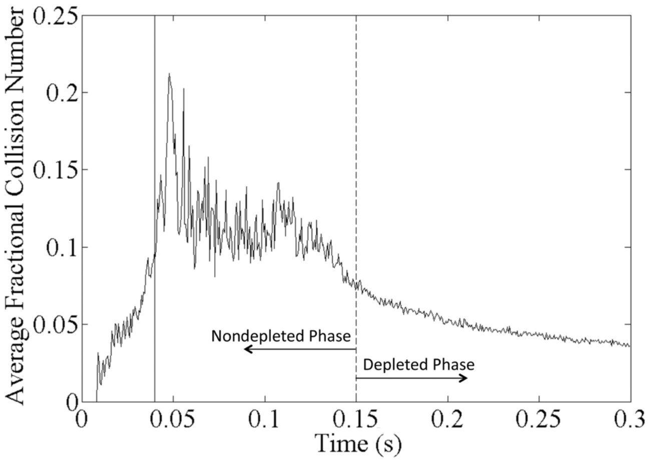

FIG. 6. Average fractional collision number.

negative; see Fig. 5). It would appear that a pseudo-steady-state has been achieved and lasts until nearly all particles are depleted from the regolith layer. This steady state can be most easily seen in Fig. 7, which superimposes the cumulative erosion number and fractional collision number on the same time axis. The key finding, however, is that a significantly large fraction of particles are engaging in collisions, which means that interparticle collisions likely influence the erosion and ejection dynamics heavily, which will be discussed in the next section.

Further evidence of correlations between the collision dynamics and erosion dynamics is illustrated in Fig. 7. This figure shows the cumulative erosion number (Fig. 4) and average fractional collision number (Fig. 6) as a function of time and superimposed on the same plot. The variations in the erosion dynamics are very well correlated with the variations in the collision dynamics. Specifically, the collision phase of the erosion corresponds to a time when the average fractional collision number is approximately constant.

B. Collisionless DEM

In order to directly analyze the influence of collisions on the erosion rate, a "collisionless" version of the DEM was implemented such that particle trajectories could cross without collisions being resolved [Eq. (1) *sans* $\mathbf{F}_{\mathrm{Coll}}$]. The cumulative erosion number plot comparing the collisionless DEM and the original DEM model is displayed in Fig. 8. It is clear that when the collisions are removed from the simulation, the negative erosion disappears as well, which is consistent with the explanation provided above that for the system under consideration here, negative erosion (sedimentation) can only arise from collisions.

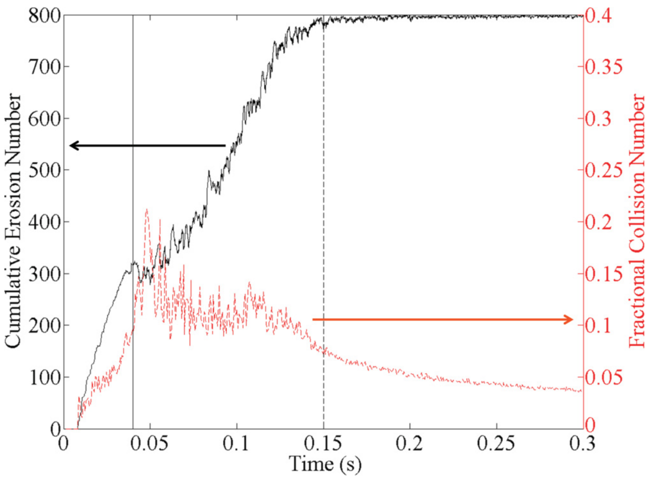

FIG. 7. (Color online) Direct comparison between erosion and collision dynamics.

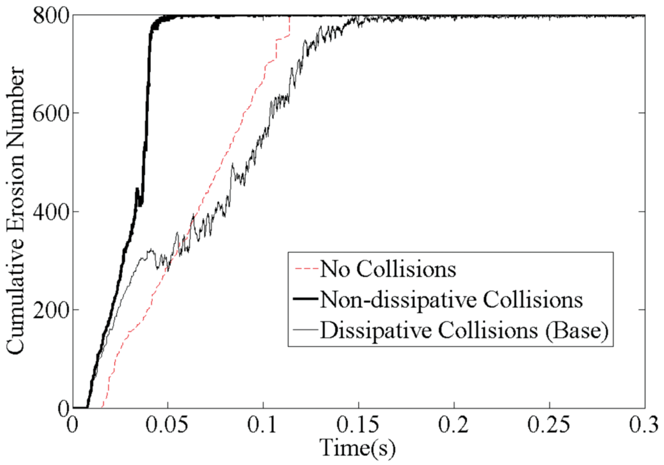

FIG. 8. (Color online) Cumulative erosion number for no collisions, nondissipative collisions, and dissipative collisions.

In addition to the disappearance of negative erosion from the plot, it can be seen from Fig. 8 that the erosion rate increases for the collisionless case compared to dissipative collisions, but increases even further when there are nondissipative collisions (i.e., $e_{\mathrm{norm}} = 1$ and $\mu = 0$). One way to explain this trend is the effect that collisions have on the particle velocities. As a simple explanation, consider the isolated case of two particles separated vertically, where the top particle is stationary and the bottom is moving upwards. If the collision is elastic, then the particles will undergo a momentum swap, leaving the top particle moving up and the bottom particle stationary (ignoring the role of lift, for purposes of illustration). Such a configuration lends itself to a high erosion rate because the top particle erodes while the bottom particle is now more likely to be involved in a collision with a particle below it. However, if the collision is inelastic, then not only will the top particle erode slower, but the bottom particle will also be less likely to be involved in another collision and thus receives less momentum from particles below it (since inelasticity causes a reduction in the relative velocity between particles upon collision). This phenomenon creates a narrower velocity distribution and thus results in fewer collisions, which was confirmed by examining the velocity distribution and collisional data (data not shown for sake of brevity). In particular, these results indicate that the rate at which collisions occur between the anchoring and erosion planes is much higher for the nondissipative case as opposed to the dissipative case (during the erosion and sedimentation phase). It is interesting to note that the erosion is so fast in the nondissipative case that the sedimentation (negative slope) is rarely observed in Fig. 8. However, the sedimentation of particles does result in the erosion rate of the dissipative case being less than that of the collisionless case. The lower erosion rate is caused by particles having difficulty moving beyond the region immediately above the erosion plane because the other particles in that region block them from moving upwards (unlike the collisionless case) until enough of the particles in this region are carried away by the plume. It is generally held that saltation, which involves particles being ejected from a granular "bed" and then returned, enhances erosion rate [9]. However, for the case studied here, the opposite is true, at least for the dissipative case examined, because the erosion rate increases when the dissipative collisions are turned off. However, typical terrestrial saltation involves a much slower gas (typically wind) and thus a smaller lift. The smaller lift means that in terrestrial saltation, the primary mechanism in which particles are lifted from the bed is collisions, whereas in our simulations it is the lift from the plume that dominates. In addition, terrestrial saltation results in a much lower density of particles above the settled bed and thus many fewer collisions occur as compared to our case: Each particle has only a possibility of being engaged in a collision in the case of saltation, whereas all particles in our case engage in many collisions [11–14]. These mid-air collisions in the case of saltation serve to decrease the number of particles returning to the surface, whereas they increase the number of particles returning in this system. It has also been shown that it may be possible to ignore the mid-air collisions for saltation without significantly changing the results [14]. Ultimately, the interparticle collisions play an entirely different role in the erosion from an impinging rocket on the Moon when compared with terrestrial saltation.

The sudden increase in the cumulative erosion number in the "no collisions" plot in Fig. 8 at $t \approx 0.125$ s is noteworthy, as well as the delay of the onset of erosion ($t \approx 0.02$ s; compared to both cases with collision). The former occurs because the particles at the bottom of the bed are arranged in a monolayer. Since there are no collisions to disrupt this monolayer, and there is no dependence of the vertical forces on the particles in the x or z directions, these particles remain in a monolayer and all erode at exactly the same time. The delay of the onset of erosion is caused by a lack of momentum transfer between particles. Particles can only gain momentum from the plume and cannot transfer that momentum to a more "useful" particle (i.e., one nearer to the top of the bed); i.e., the top layer of particles will erode first, and in the "no collisions" case their only source of momentum is drag/lift, whereas in either of the "collisions" cases, momentum can also be transferred via collisions from particles lower in the bed to these top layers.

C. Effect of input parameters

The parameter space can be broadly divided into three categories: plume properties, system properties, and particle properties. Depths of the plume penetration into the regolith, the initial height of the erosion plane, and the particle restitution coefficient denote an example from each of these categories, respectively. In general, by studying the effect of various parameters on cumulative erosion number and instantaneous collision number over time, the role of various parameters on erosion dynamics is assessed.

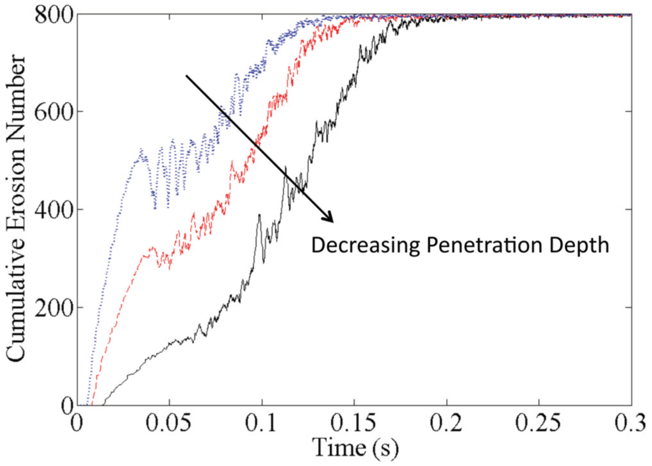

FIG. 9. (Color online) Cumulative erosion number for different anchoring plane depths. Penetration depths are 2, 4 (base case), and 6 particle diameters. All other parameters are given in Table II.

1. Plume properties: Penetration depth

As described previously, the anchoring plane denotes the initial depth of penetration of the gas plume into the regolith. Physically, this penetration depth depends on the permeability of the regolith. Specifically, a larger permeability of the regolith will lead to greater penetration depth of the gas plume. Figure 9 depicts the effect of varying the initial anchoring plane on the overall erosion rate. As expected, the overall erosion rate increases as the penetration depth increases. In other words, a more permeable regolith will exhibit a significantly higher erosion rate than a less permeable one.

2. System properties: Location of the erosion plane

Even though changing the height of the erosion plane above the regolith layer does not affect the particles at all, doing so can yield valuable insight into the erosion dynamics. As described before, the erosion plane in the base case is located at one particle diameter above the top of the regolith layer, which is useful for calculating the erosion rate very close to the surface. For comparison, Fig. 10 contains the cumulative

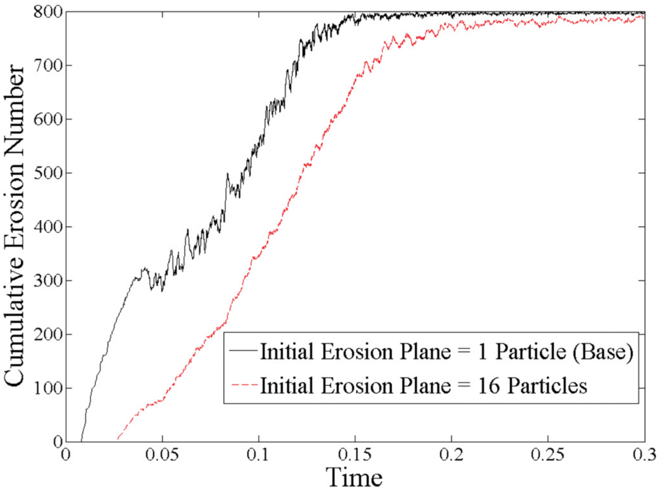

FIG. 10. (Color online) Cumulative erosion number for different erosion plane heights.

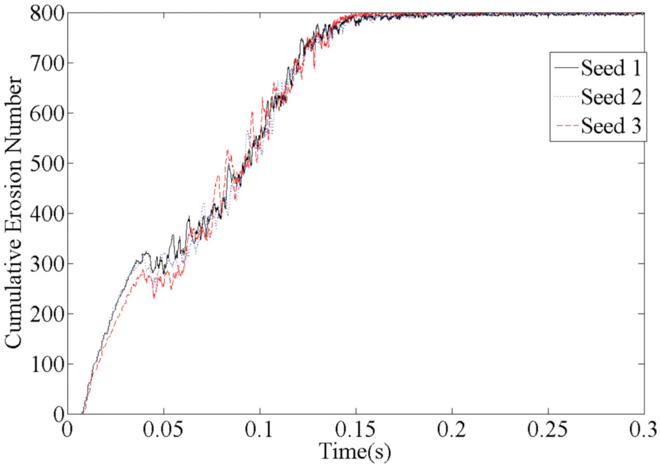

FIG. 11. (Color online) Sensitivity of cumulative erosion number to seed used for initial particle configuration. Seed 1 refers to base case (Fig. 4); parameters used for all seeds given in Table II.

erosion number plot for two different locations of the erosion plane. As one expects, the overall erosion rate (average slope; see Fig. 4) is lower for a higher erosion plane because it takes longer for the particles to get to an erosion plane that is higher. Perhaps more importantly from a physical standpoint, it is observed that as the erosion plane is moved away from the regolith, the negative erosion in the plot (i.e., the portions with negative slope) diminishes greatly in size. In the results shown here, the negative erosion almost disappears for the erosion plane that is located at 16 particle diameters ($y = 3.0$ cm initially) from the surface of the regolith. This disappearance of the negative erosion as the erosion plane moves away from the regolith surface is caused by a significant reduction in the number of collisions as the particles move away from the regolith surface. Fewer collisions results in fewer opportunities for particles to travel downwards and cross an erosion plane that is located farther from the regolith surface.

3. *Particle properties*

The other parameters for which a sensitivity analysis was performed include the initial particle arrangement, size of periodic domain, spring constant, coefficient of restitution, and particle friction. As is apparent in Fig. 11, starting with a different initial particle configuration (as a result of settling from a different initial state) does not change the overall erosion rate, although small deviations in the plots do exist, as is expected from a different initial state. Similarly, by varying the size of the periodic box in the x and z directions, the approximate flux of particles (erosion rate per unit area) does not show any change as seen in Fig. 12. In addition, starting with a different number of particles results in the same qualitative behavior as plotted in Fig. 13. The erosion-only phase lasts for the same amount of time, as is expected, but the erosion-and-sedimentation phase lasts longer because more particles are available for erosion.

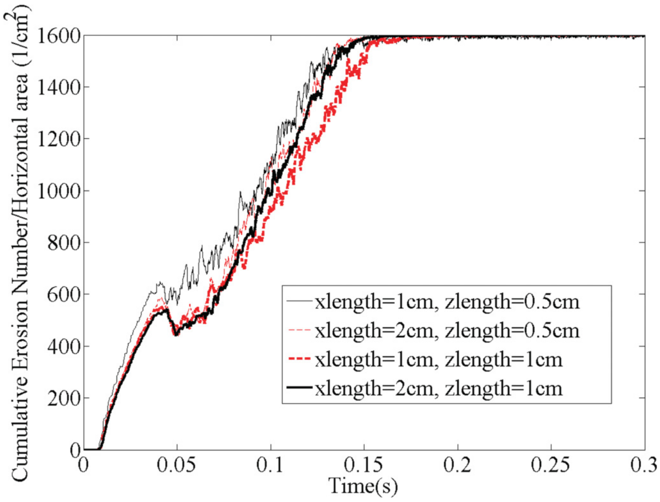

FIG. 12. (Color online) Cumulative erosion number per box area versus time for different periodic domain sizes. Note that the number of particles in each simulation is scaled based on the area (linearly compared to base case parameters). All other parameters for all cases are shown in Table II.

Changes in the spring constant result in qualitative and quantitative changes in the cumulative erosion plot. Figure 14 gives the cumulative erosion number versus time for spring constants higher than that used in the base case. Note that only larger spring constant values are tested because it is known that smaller values result in particles that are much "softer" than actual regolith. The figure shows that with higher spring constants than the one used in the base case ($k = 8 \times 10^6$ g cm/s^2), a dip in the cumulative erosion number is observed at the beginning of the collision phase of erosion, as well as a decrease in the overall erosion rate. These phenomena can be explained by a shorter collision duration [see Eq. (30)], which results in a higher collision frequency. The more collisions that occur, the more likely that the collisions will result in particles traveling back below the erosion plane. It is interesting to note that the amount of kinetic energy in the system is actually larger for a higher spring coefficient even though more collisions are occurring (each collision dissipates energy and thus one might assume more collisions would result in more energy dissipated; figure not shown for sake of brevity). This trend may have to do with instabilities (such

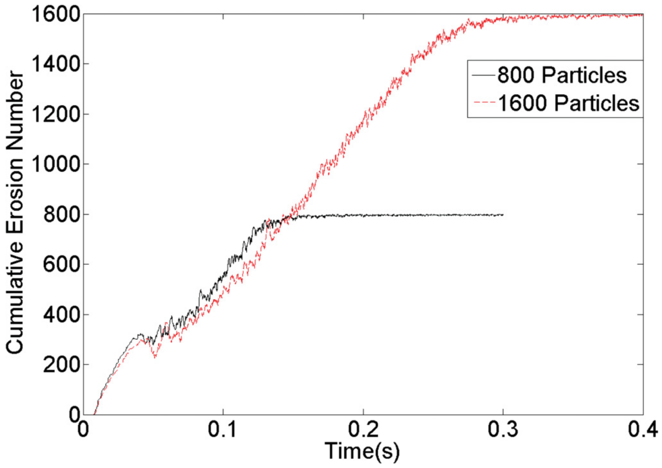

FIG. 13. (Color online) Cumulative erosion number for two different initial bed depths (number of particles). All other parameters are shown in Table II.

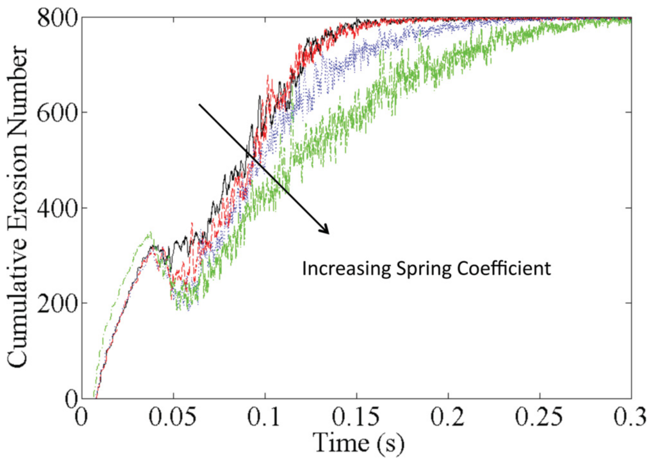

FIG. 14. (Color online) Cumulative erosion number versus time for different spring coefficients. Spring coefficients depicted are 8×10^6 (base case), 8×10^7, 8×10^8, and 8×10^9.

as clusters) forming in the system, which have been shown in other systems to result in less energy dissipation, on average, in each collision [28]. The most important finding here is that the qualitative nature of our conclusions does not change with significant changes of the spring constant used.

Changes in both the coefficient of restitution and friction coefficient have significant effects on the erosion, as is evident from Fig. 15. Of particular interest is the significant difference in how the erosion rate is affected by an increase in the friction coefficient for the two coefficients of restitution shown. The erosion rate is significantly lower for $\mu = 0.2$ when $e_{\mathrm{norm}} = 0.6$ [Fig. 15(a)] as compared to when $e_{\mathrm{norm}} = 0.8$ [Fig. 15(b)]. However, as can be seen in Fig. 15(b), this trend in which the erosion rate is higher for a lower dissipation rate is not always true because the erosion rate actually increases with an increase in the coefficient of friction. In addition to the trend in erosion rate, it is also interesting to note that the erosion-only phase of erosion has approximately the same slope for all conditions, but lasts for a different amount of time. This phenomenon also likely has to do with a lower coefficient of restitution causing a narrower velocity distribution as the duration of the erosion-only phase appears to have little dependence on the friction coefficient. In addition, by performing simulations of a single particle impacting the bed (no plume) at a high speed and shallow angle (as occurs in our simulations because the horizontal velocities are much greater than the vertical ones), we have seen that for the case in which $e_{\mathrm{norm}} = 0.6$ and $\mu = 0.2$ many fewer particles are ejected upon impact when compared with any of the other conditions in Fig. 14. This result means that for these conditions, the erosion caused by particles returning and colliding with the bed will be much smaller and thus the overall erosion rate will be much smaller. Although a full physical explanation for the results of changing dissipation is not apparent, the qualitative nature of our conclusions regarding the significance of collisions does not change.

IV. SUMMARY

The discrete element method is used to simulate the erosion of the lunar regolith caused by a landing rocket. A one-way coupling is assumed in which the exhaust plume affects the regolith but not vice versa. DEM simulations of monodisperse particles are used to calculate the erosion rate and collision characteristics of the particles at a distance 6 m away from the impingement point.

The DEM results establish that interparticle collisions play an important role in the eroding layer and lead to negative erosion (sedimentation) in the system. The amount of negative erosion changes with the height of the erosion plane, suggesting that once particles leave the area near the surface, they rarely return. This result implies that the single-particle trajectories calculated in the PET model can be adequate, if and only if the particle trajectories are calculated sufficiently high above the surface where collisions are no longer dominant and if they are seeded with a realistic distribution of initial velocities representing the scattering caused by the collisions. In this model, the minimum height appropriate for trajectory calculations is only about 16 particle diameters above the surface, but more detailed simulations will be needed to fine-tune this estimate. In addition, as many as 20% of eroded particles are observed to be involved in a collision at a given time.

A direct analysis of the influence of collisions on the erosion rate is achieved via comparison with a collisionless DEM model. The results show that the erosion rate is highest for nondissipative collisions, followed by the no-collisions case, and then the dissipative base case. Nondissipative collisions result in the largest erosion rate because collisions serve as an effective means of transferring momentum between particles

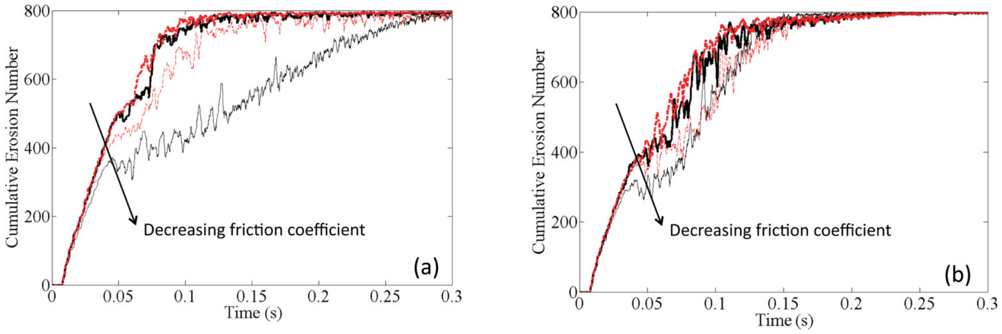

FIG. 15. (Color online) Cumulative erosion number versus time for different coefficients of restitution and friction coefficient. (a) $e_{\mathrm{norm}} = 0.6$, (b) $e_{\mathrm{norm}} = 0.8$. Friction coefficients displayed are 0.2 (base case), 0.5, 0.8, and 1.4.

via a perfect swap of momentum. For the (simplistic) case of a perfectly vertical collision, this momentum swap leads to one particle traveling quickly upwards (thus eroding quicker), while the second, slower particle remains lower in the plume and thus can more easily be involved in a collision with another particle. However, dissipative collisions (for the base case examined, as well as more dissipative systems) result in a smaller relative outbound velocity and thus neither particle gains a large boost, but both are located higher in the plume and thus are less likely to be involved in a collision with a particle coming from below and thus will erode slower. Finally, the collisionless case is neither helped by a momentum swap between particles nor hindered by an inefficient momentum exchange, which results in an erosion rate between the other two cases. These results are not consistent with what one might expect based on terrestrial saltation, in which a wind carries sand grains. For terrestrial saltation, the collisions between grains on the surface account for much of the erosion (grains coming down and eroding other grains) and so one might expect collisions to increase the erosion rate. However, because collisions take place above the surface in our system and because of the much higher lift force, this is not the case.

It is important to note that although the PET model implicitly includes collisions in the erosion rate model (E of PET; trajectories, T, do not consider interparticle interactions), there are insufficient data to determine how accurate the erosion rate is over a wide variety of conditions. Experiments with scour holes forming under a jet have a geometry where the erosion takes place only on the rim and therefore have too little downwind surface area for colliding particles to continue interacting with the eroding surface [8]. Therefore, while such experiments are helpful to measure initial lift rates due to the aerodynamic forces in isolation, measurements of the overall erosion rate as modified by the feedback mechanisms of mid-air particle collisions cannot be made. Such experiments are useful for their compactness in situations such as reduced-gravity aircraft to provide a first-order estimate (at best) of erosion-rate scaling, but higher fidelity experiments are needed to incorporate collisions, which we now know are important to the physics of lunar soil erosion. By modeling the erosion explicitly, one can obtain a more accurate estimate of the erosion rate than in experiments to date.

An examination of the effect of different parameters on the overall erosion rate suggests that the permeability of the regolith (penetration depth of the plume) is the most important system parameter that affects the erosion dynamics. However, the coefficient of restitution and the friction coefficient also have a significant effect on the erosion rate because they change how each collision affects the erosion rate. The spring coefficient also has a quantitative effect on the erosion rate because the duration of each collision changes. In addition, periodic box dimensions and initial settling condition have negligible effect on global erosion rate. None of these parameters, however, change the qualitative conclusions drawn above.

This work represents a first step in establishing the important role of collisions in the erosion and ejection dynamics of regolith spurred by a lunar landing. An important extension of the current effort is to consider the polydisperse nature of the regolith material, since this polydispersity will not only impact collision rates of (unlike) particles, but also lead to species segregation.

ACKNOWLEDGMENTS

A.A. is grateful to Sofiane Benyahia at NETL for his support with MFiX. The authors are grateful to Xiaoayi Li for the CFD work used to generate the plume velocity profile. Funding for this work was provided by the National Aeronautics and Space Administration (Grant No. NNX09AD07A). This work was also supported by a NASA Office of the Chief Technologist's Space Technology Research Fellowship (Grant No. NNX11AM71H).

APPENDIX

In this appendix we present the drag and lift coefficients (developed by Loth [25,26]) used in the DEM simulations. The drag coefficient is defined by the following piecewise function:

$$C_{\mathrm{Drag}} = \frac{C_{D,\mathrm{Kn},\mathrm{Re}}}{(1+\mathrm{Ma}^4)} + \frac{\mathrm{Ma}^4 C_{D,fm,\mathrm{Re}}}{1+\mathrm{Ma}^4} \quad \text{for Re} < 45, \tag{A1}$$

$$C_{\mathrm{Drag}} = \frac{24}{\mathrm{Re}}[1+0.15\mathrm{Re}^{0.687}]H_m + \frac{0.42C_M}{1+\frac{42500G_M}{\mathrm{Re}^{1.16}}} \quad \text{for Re} \geqslant 45. \tag{A2}$$

Re is the particle Reynolds number defined as

$$\mathrm{Re} = \frac{\rho v_0 d}{\mu}, \tag{A3}$$

where ρ is the gas density, v_0 is the magnitude of the relative unhindered velocity [see Eq. (29)], d is the diameter of the particle, and μ is the gas viscosity. Ma is the Mach number defined as

$$\mathrm{Ma} = \frac{v_0}{\sqrt{\gamma R T}}, \tag{A4}$$

where R is the gas constant, γ is the ratio of specific heats for the gas, and T is the temperature of the gas. The constant $C_{D,\mathrm{Kn},\mathrm{Re}}$ is defined as

$$C_{D,\mathrm{Kn},\mathrm{Re}} = \frac{\frac{24}{\mathrm{Re}}(1+0.15\mathrm{Re}^{0.637})}{1+(2.514+0.8e^{(-0.55/\mathrm{Kn})})\mathrm{Kn}}, \tag{A5}$$

where the Knudsen number, Kn, is defined as

$$\mathrm{Kn} = \sqrt{\frac{\pi\gamma}{2}}\frac{\mathrm{Ma}}{\mathrm{Re}}. \tag{A6}$$

The constant $C_{D,fm,\mathrm{Re}}$ is defined as

$$C_{D,fm,\mathrm{Re}} = \frac{C_{D,fm}}{1+\left(\frac{C_{D,fm}}{1.63}-1\right)\sqrt{\frac{\mathrm{Re}}{45}}}. \tag{A7}$$

The constant $C_{D,fm}$ is defined as

$$C_{D,fm} = \frac{(1+2s^2)e^{-s^2}}{s^3\sqrt{\pi}} + \frac{(4s^4+4s^2-1)\mathrm{erf}(s)}{2s^4} + \frac{3}{2s}\sqrt{\pi\frac{T_p}{T_\infty}}, \tag{A8}$$

where T_p is the temperature of the particle and T_∞ is the temperature of the gas, which are assumed to be equal to each other. The constant s is defined as

$$s = \mathrm{Ma}\sqrt{\frac{\gamma}{2}}. \tag{A9}$$

The constant $C'_{D,fm}$ is defined as

$$C'_{D,fm} = C_{D,fm,T_p=T_\infty} = \frac{(1+2s^2)e^{-s^2}}{s^3\sqrt{\pi}} + \frac{(4s^4+4s^2-1)\mathrm{erf}(s)}{2s^4}. \tag{A10}$$

H_m is defined as

$$H_m = 1 - \frac{0.258C_m}{1+514C_m}. \tag{A11}$$

C_m is defined in two ways, depending on the Mach number:

$$C_m = \frac{5}{3} + \frac{2}{3}\tanh\left[3\ln\left(\mathrm{ReKn}\sqrt{\frac{2}{\pi\gamma}} + 0.1\right)\right] \quad \text{for Ma} \leqslant 1.45, \tag{A12}$$

$$C_m = 2.044 + 0.2\exp\left\{-1.8\left[\ln\left(\frac{2}{3}\mathrm{ReKn}\sqrt{\frac{2}{\pi\gamma}}\right)\right]^2\right\} \quad \text{for Ma} < 1.45. \tag{A13}$$

G_m is defined in two ways, depending on the Mach number:

$$G_m = 1 - 1.525\mathrm{Ma}^4 \quad \text{for Ma} \leqslant 0.89, \tag{A14}$$

$$G_m = 0.0002 + 0.0008\tanh\left[12.77\,(\mathrm{Ma} - 2.02)\right] \quad \text{for Ma} > 0.89. \tag{A15}$$

The lift coefficient is defined as

$$C_{\mathrm{Lift}} = \frac{12.92}{\pi}J^*\sqrt{\frac{\omega^*_{\mathrm{shear}}}{\mathrm{Re}}} + \Omega^*_p C^*_{L\Omega}. \tag{A16}$$

J^* is defined as

$$J^* = 0.3\left\{1 + \tanh\left[\frac{s}{2}\left(\log_{10}\left[\sqrt{\frac{\omega^*_{\mathrm{shear}}}{\mathrm{Re}}} + 0.191\right]\right)\right]\right\} \times \left\{\frac{2}{3} + \tanh\left[6\sqrt{\frac{\omega^*_{\mathrm{shear}}}{\mathrm{Re}}} - 1.92\right]\right\}. \tag{A17}$$

$\omega^*_{\mathrm{shear}}$ is the continuous-phase vorticity and is defined as

$$\omega^*_{\mathrm{shear}} = \left|\frac{(Dv_0)\,d}{v_0}\right|, \tag{A18}$$

where Dv_0 is the component of the gradient of the plume velocity field perpendicular to v_0 (taken, for convenience, to be the y component, perpendicular to the surface of the regolith) and d is the particle diameter. Ω^*_p is the nondimensional particle rotation rate defined as

$$\Omega^*_p = \frac{(Dv_0)\,d}{2v_0}. \tag{A19}$$

$C^*_{L\Omega}$is defined as

$$C^*_{L\Omega} = 1 - \{0.675 + 0.15(1 + \tanh[0.28(\Omega^*_p - 2)])\} \times \tanh[0.18\mathrm{Re}^{0.5}]. \tag{A20}$$

---

[1] L. D. Jaffe, Science **171**, 798 (1971).

[2] B. J. O'Brien, S. C. Freden, and J. R. Bates, J. Appl. Phys. **41**, 4538 (1970).

[3] P. T. Metzger, J. E. Lane, C. D. Immer, and S. Clements, in *Lunar Settlements*, edited by Haym Benaroya (CRC Press, Boca Raton, FL, 2010), pp. 551–576.

[4] A. B. Morris, D. B. Goldstein, P. L. Varghese, and L. M. Trafton, in *Proc. of the 27th Intl. Symposium on Rarefied Gas Dynamics*, Vol. 1333 (AIP, Melville, NY, 2011), pp. 1187–1192.

[5] C. Conrad, R. F. Gordon, Jr., and A. L. Bean, Apollo 12 Technical Crew Debriefing, NASA Johnson Space Center, Houston, TX, Vol. 1, pp. 9.11-9.12 (1969).

[6] D. Scott, J. Irwin, and A. Worden, Apollo 15 Technical Debriefing, Rep. MSC-4561, NASA Manned Space Center, Houston, TX, p. 9.14 (1971).

[7] P. T. Metzger and R. P. Mueller, in Mars Design Reference Architecture 5.0, Addendum, NASA SP-2009-566-ADD, pp. 234–248 (2009).

[8] P. T. Metzger, J. E. Lane, C. D. Immer, J. N. Gamsky, W. Hauslein, X. Li, R. C. Latta III, and C. M. Donahue, in *Proceedings of Earth and Space 2010, 12th Biennial ASCE Aerospace Division International Conference on Engineering, Construction, and Operations in Challenging Environments, Honolulu, HI, March 14-17* (ASCE, Reston, VA, 2010).

[9] R. A. Bagnold, *The Physics of Blown Sand and Desert Dunes* (Methuen, London, 1941).

[10] J. F. Kok, E. J. R. Parteli, T. I. Michaels, and D. B. Karam, Rep. Prog. Phys. **75**, 106901 (2012).

[11] M. Sørensen and I. McEwan, Sedimentology **43**, 65 (1996).

[12] N. Huang, Y. L. Zhang, and R. D'Adamo, J. Geophys. Res. **112**, 11 (2007).

[13] Z. Dong, N. Huang, and X. Liu, J. Geophys. Res. **110**, D24113 (2005).

[14] J. F. Kok and N. O. Renno, J. Geophys. Res. **114**, D17204 (2009).

[15] J. E. Lane, P. T. Metzger, and C. D. Immer, in *Proceedings of Earth and Space 2008, 11th Biennial ASCE Aerospace Division International Conference on Engineering, Construction and Operations in Challenging Environments, Long Beach, California, March 3-5* (ASCE, Reston, VA, 2008).

[16] J. E. Lane, P. T. Metzger, and J. W. Carlson, in *Proceedings of Earth and Space 2010, 12th Biennial ASCE Aerospace Division International Conference on Engineering, Construction and Operations in Challenging Environments, Honolulu, HI, March 14-17* (ASCE, Reston, VA, 2010).

[17] J. E. Lane and P. T. Metzger, Part. Sci. Technol. **30**, 196 (2012).

[18] P. T. Metzger, J. Smith, and J. E. Lane, J. Geophys. Res. **116**, E06005 (2011).

[19] C. Immer, P. Metzger, P. E. Hintze, A. Nick, and R. Horan, Icarus **211**, 1089 (2011).
[20] M. A. Hopkins, J. T. Jenkins *et al.*, Mech. Mater. **16**, 179 (1993).
[21] I. Goldhirsch, M.-L. Tan, and G. Zanetti, J. Sci. Comput. **8**, 1 (1993).
[22] T. Pöschel and T. Schwager, *Computational Granular Dynamics: Models and Algorithms* (Springer-Verlag, New York, 2005).
[23] P. A. Cundall and O. D. L. Strack, Géotechnique **29**, 47 (1979).
[24] R. Garg, J. Galvin, T. Li, and S. Pannala, Documentation of open-source MFIX-DEM software for gas-solid flows, from https://mfix.netl.doe.gov/documentation/dem_doc_2010.pdf.
[25] E. Loth, AIAA J. **46**, 801 (2008).
[26] E. Loth, AIAA J. **46**, 2219 (2008).
[27] K. F. Malone and B. H. Xu, Particuology **6**, 521 (2008).
[28] R. Brito and M. H. Ernst, Europhys. Lett. **43**, 497 (1998).
[29] See https://mfix.netl.doe.gov/.